buildings

MDPI

Article

Time-Dependent Behavior of Composite Steel–Recycled Aggregate Concrete Beams via Thermomechanical Finite Element Modeling

Jinsheng Yang [1], Changyong Liu [2,3,*], Qinghe Wang [4] and Yue Geng [2,3]

[1] School of Civil Engineering, Harbin Institute of Technology, Harbin 150090, China; yangjinsheng@stu.hit.edu.cn
[2] Key Laboratory of Structures Dynamic Behavior and Control of the Ministry of Education, Harbin Institute of Technology, Harbin 150090, China; gengyue@hit.edu.cn
[3] Key Laboratory of Smart Prevention and Mitigation of Civil Engineering Disasters of the Ministry of Industry and Information Technology, Harbin Institute of Technology, Harbin 150090, China
[4] School of Civil Engineering, Shenyang Jianzhu University, Shenyang 110168, China; wangqinghe@sjzu.edu.cn
* Correspondence: liuchangyong@hit.edu.cn; Tel.:+86-0451-8628-2084

Abstract: This paper aims to investigate the impact of recycled coarse aggregate (RCA) on the time-dependent behavior of composite steel–recycled aggregate concrete (RAC) beams. The FE models of the composite beams were established, and a parametric study was conducted to obtain the primary factors. Furthermore, the design method for predicting the long-term deflection was proposed by including the shrinkage deflection component. The results showed that the RCA replacement ratio significantly influenced the long-term deflection of composite beams; the long-term deflection of composite beams with 100% RCA increased by 3.5–17.2% compared with those without RCA. Moreover, using uniform shrinkage and creep models led to a 4.5–10.3% overestimation of the long-term deflection of the composite beams with the composite slabs due to nonuniform shrinkage and creep distributions. Finally, the proposed design procedures could accurately predict the long-term deflection of the composite steel–RAC beams, and the difference between the calculated and FE results ranged from 0.961 to 0.986.

Keywords: composite steel–concrete beam; recycled aggregate concrete; long-term behavior; finite element modeling; design procedure

Citation: Yang, J.; Liu, C.; Wang, Q.; Geng, Y. Time-Dependent Behavior of Composite Steel–Recycled Aggregate Concrete Beams via Thermomechanical Finite Element Modeling. *Buildings* **2022**, *12*, 756. https://doi.org/10.3390/buildings12060756

Academic Editor: Marco Di Ludovico

Received: 26 April 2022
Accepted: 30 May 2022
Published: 1 June 2022

1. Introduction

Composite steel–concrete beams are primarily composed of steel beam, slab, and shear connector components [1], as shown in Figure 1a. The typical slabs also include reinforced concrete (RC) slabs and composite slabs. In the composite slabs, the open-trough steel decks, clip-pan steel decks, and streel-bar truss decks are generally selected (see Figure 1b–d) [2]. To date, composite steel–concrete beams have been widely used in industrial and residential constructions, with the typical concrete strength in the range of 20–40 MPa [3]. In this context, composite steel–concrete beams are potential structural members to use recycled aggregate concrete (RAC). Due to the residual mortar adhered to the surface of recycled coarse aggregate (RCA), RAC exhibits inferior mechanical properties to natural aggregate concrete (NAC); however, it is feasible to obtain RAC with a compressive strength of 20–40 MPa [4–7]. Current studies on the ultimate behavior of composite beams have demonstrated that composite beams using 100% RAC can have a flexural behavior that is similar to composite beams using NAC [8], with a 1.0% decrement in the flexural strength and 5.5% decrement in the flexural stiffness.

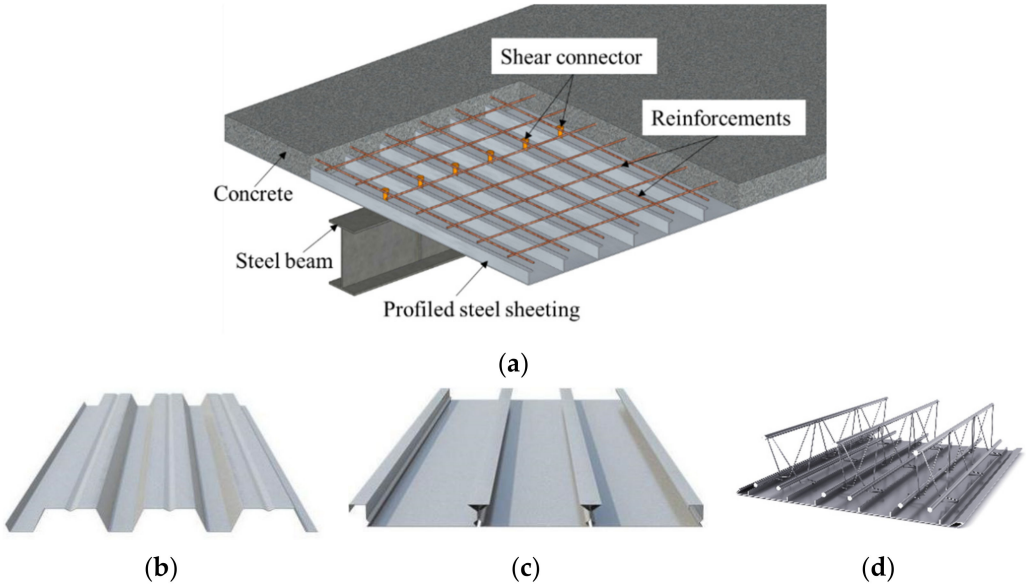

Figure 1. Typical composite steel–concrete beams with (**a**) a schematic of composite steel–concrete beams using composite slabs, (**b**) an open-trough deck, (**c**) a clip-pan deck, and (**d**) a steel-bar truss deck.

In addition to the ultimate behavior of composite beams, their serviceability should be concentrated because RAC exhibits 27.6–77.0% higher shrinkage and 23.0–120.0% higher creep deformation than NAC [9–13]. It is also worth mentioning that the time-dependent behavior is not adequately considered, even for composite steel–NAC beams, in current international standards as their spans are traditionally limited. Increasingly larger spans are specified for composite beams, and the effects of long-term shrinkage and creep on the time-dependent behavior of composite steel–concrete beams are significant. To date, the investigations into the time-dependent behavior of composite steel–NAC beams have primarily focused on (a) the effects of long-term shrinkage and creep and (b) the degree of shear connection on the time-dependent behavior of composite beams.

Significant effects of shrinkage and creep on the time-dependent behavior of composite beams have been reported. Researchers recorded additional deflection (δ_{cs}) due to shrinkage and creep effects, accounting for 1.2–4.0 times the instantaneous deflection (δ_{inst}) [14–17], which was higher than the values recommended by international specifications. Sequentially, Wright et al. [18] proposed a prediction method to calculate the additional shrinkage curvature of composite beams. Ranzi et al. [19], Reginato et al. [20], Erkmen et al. [21], and Xiang et al. [22] quantified the effects of shrinkage and creep on the long-term deflection of composite beams and proposed methods for predicting long-term deflection. The above investigations on composite beams used uniform shrinkage and creep models; that is, the relative humidity inside concrete slabs was considered to be identical to the ambient relative humidity. This assumption is believed to be acceptable for composite beams using solid RC slabs, as shown in Figure 2a, where moisture can diffuse on the RC slabs from both the top and bottom surfaces. However, the distribution of the relative humidity of the composite beams with composite slabs is nonuniform throughout the thickness of their slabs due to the impermeable surface of their slabs (Figure 2b), correspondingly leading to nonuniform shrinkage and creep deformations. Al-deen et al. [23] measured the distribution of the relative humidity over the thickness of composite slabs, and the relative humidity at the bottom surface was at a high level even after 124 days. Ranzi et al. [24] compared the time-dependent deflection of composite beams using nonuniform and uniform shrinkage distributions and highlighted that nonuniform shrinkage models should be used in the routine design procedures. Recently, they measured the shrinkage distributions in the solid slabs and composite slabs using RCA and proposed

nonuniform relative humidity and corresponding shrinkage models for composite slabs with RCA [2,25–29].

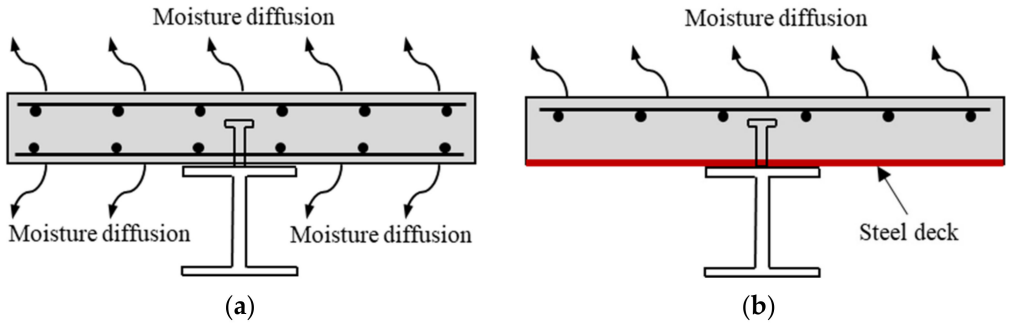

Figure 2. The humidity transfer of composite steel–concrete beams with (**a**) composite beams with RC slabs and (**b**) composite beams with composite slabs.

In actual practice, the partial shear connection is generally selected for composite beams, and the time-dependent flexural stiffness decreases over time due to the slip between the steel beam and slab [30,31]. Al-deen et al. reported an increment of 34.8–58.2% in the additional slip due to shrinkage and creep effects compared with the slip under instantaneous loading [23]. A remarkable difference ranging from −30% to +90% between the predicted and measured data was noticed when the influence of the additional slip was not considered. Oehlers et al. [32] proposed a calculation method for the flexural stiffness of composite beams considering the strength and ductility of shear connectors. Liu et al. [33] proposed a method for calculating the shear-slip strain difference of steel–concrete composite beams based on the elastic theory. Nie et al. [34] proposed a design method to predict flexural stiffness considering the slip effects. Fu et al. [35] proposed a stiffness calculation method for the partial shear connections of composite beams based on experimental and theoretical analysis. Yuan et al. [36] adopts the numerical analysis method to put forward a simplified formula of the stiffness reduction coefficient of composite beams. The flexural stiffness decreased while the time-dependent slip increased with the incorporation of RCA. In both cases, including the composite beams using RC slabs (uniform shrinkage and creep distributions) and those using composite slabs (nonuniform shrinkage and creep distributions), the influence of the degree of shear connection on the time-dependent behavior of the composite steel–RAC beams should be quantified.

To sum up, scholars have focused on the long-term performance of composite beams using RC slabs via experimental and finite element (FE) modeling. However, the influence of nonuniform shrinkage and creep on the long-term behavior has yet to be quantified for composite beams with composite slabs. Furthermore, no study has investigated the long-term performance of steel–RAC beams, which hinders the structural application of RAC.

In this context, the long-term performance of steel–RAC beams was studied according to the RCA replacement ratio and composite floor type (uniform shrinkage/nonuniform shrinkage). This study aimed to quantify the combined effects of the cracking, shrinkage, creep, and degree of shear connection of concrete on the time-dependent behavior of composite steel–RAC beams and propose their routine design procedures. To this end, FE models of the time-dependent behavior of the composite beams were established using Abaqus software. The shrinkage effect was simulated by applying a temperature field to the concrete slabs, and the creep effect was predicted by the age-adjusted effective modulus method (AEMM). The FE models were benchmarked against available time-dependent flexural and push-out test results from full-scale composite beams with RC or composite slabs. A parametric study was further conducted to quantify the influence magnitude of the various factors on the time-dependent behavior of composite steel–RAC beams. The design procedures for estimating the long-term deflection of composite beams were proposed and evaluated by the numerical data. The research content of this paper fills the

gap in the long-term performance of steel–RAC beams, and further promotes the structural application of RAC.

2. Establishing FE Models

The FE models of the time-dependent behavior of composite steel–concrete beams were proposed using Abaqus software, as shown in Figure 3. The FE model included a steel beam component, a concrete slab component, profiled steel decking in the composite slab, reinforcements, and shear connectors. A temperature field was determined and applied to the concrete slab to simulate the long-term shrinkage effect, and the AEMM was employed to reflect the creep effect.

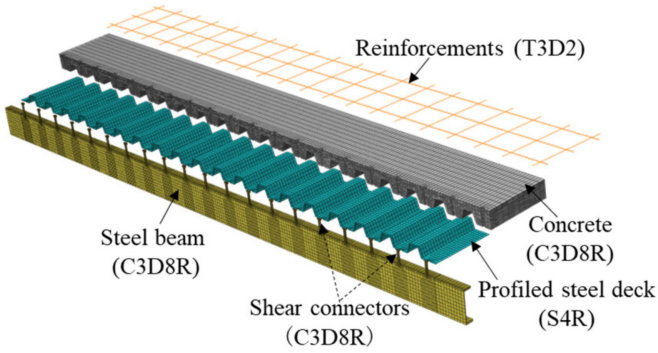

Figure 3. The FE model of a typical composite steel–concrete beam (a semi-model).

2.1. Materials

2.1.1. Steel

For the serviceability behavior of composite beams, the steel components were generally in the elastic stage [16,23]. However, for the case that the composite beams with large spans suffered high loads, the whole stress–strain relationship of the steel components was included in the FE models.

Profiled Steel Decks

The profiled steel decks were generally produced with a thickness of 0.5–1.2 mm and exhibited a similar yield and ultimate strength. In this case, the elastic–perfectly plastic model was selected for the profiled steel decks, as shown in Figure 4.

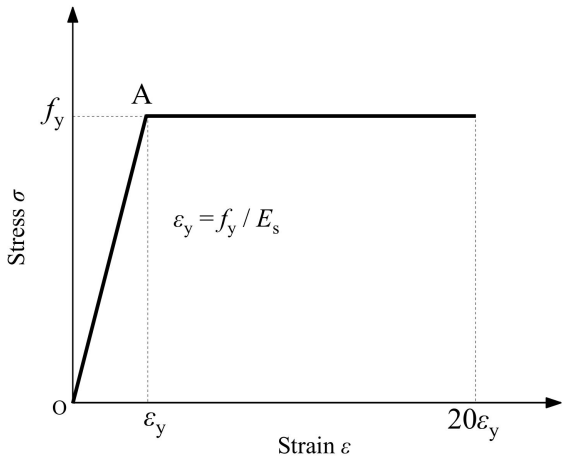

Figure 4. The stress–strain curve of the profiled steel decks.

Steel Beam, Reinforcements, and Shear Connectors

The elastoplastic stress–strain (σ–ε) model suggested by Katwal et al. [37] was used for the steel beam, reinforcements, and shear connectors, as shown in Figure 5. Equation (1) expresses the specific relations:

$$\sigma = \begin{cases} E_s\varepsilon & 0 \le \varepsilon < \varepsilon_y \\ f_y & \varepsilon_y \le \varepsilon < \varepsilon_p \\ f_u - (f_u - f_y) \cdot (\frac{\varepsilon_u - \varepsilon}{\varepsilon_u - \varepsilon_p})^p & \varepsilon_p \le \varepsilon < \varepsilon_u \\ f_u & \varepsilon_u \le \varepsilon \end{cases} \quad (1)$$

where E_s is the elastic modulus of steel; f_y and f_u represent the yield and ultimate strength of steel, respectively; ε_y indicates the strain under the yield strength; ε_p and ε_u stand for the corresponding strains under the plastic strength and ultimate strength, respectively, and can be calculated by Equations (2) and (3):

$$\varepsilon_p = [15 - 0.018(f_y - 300)]\varepsilon_y \quad (2)$$

$$\varepsilon_u = [100 - 0.15(f_y - 300)]\varepsilon_y \quad (3)$$

where p is the hardening index and E_p indicates the elastic modulus in the plastic stage:

$$p = E_p(\frac{\varepsilon_u - \varepsilon_p}{f_u - f_y}) \quad (4)$$

$$E_p = 0.02E_s \quad (5)$$

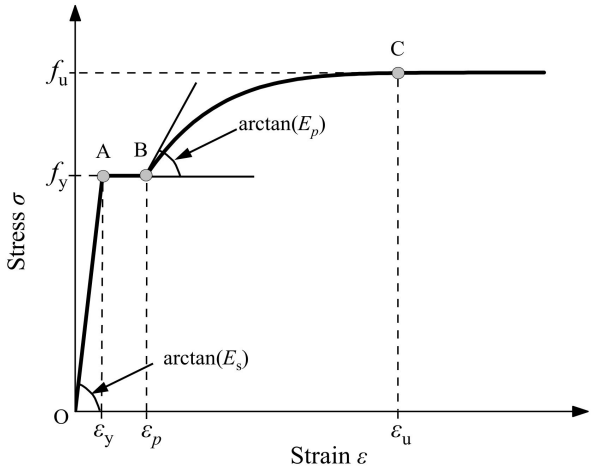

Figure 5. The stress–strain curve of the steel beam, studs, and reinforcements.

2.1.2. Concrete

The concrete damaged plasticity (CDP) model was specified for natural concrete and RAC. The primary parameters included the elastic modulus (E_c), the dilation angle (ψ), the flow potential eccentricity (e), the ratio of the compressive strength under biaxial loading to the uniaxial compressive strength (f_{b0}/f'_c), the ratio of the second stress invariant on the tensile meridian to that on the compressive meridian (K_c), the viscous parameter (u), and the stress–strain curves of concrete under tension and compression. Mainly, ψ was usually in the range of 30°–45°, and this study selected a value of 35°; we also used the default values of e, f_{b0}/f'_c, and K_c equaling 0.1, 1.16, and 0.667, respectively, and assigned a value of 0.005 to the viscous parameter. These five parameters follow those recommended by Katwal et al. [37] to predict the flexural behavior of composite beams. As the composite beams suffered both immediate and long-term loads, the short- and long-term material models are introduced in the following sections.

Short-Term Properties

1. Elastic Modulus

The elastic modulus of NAC ($E_{c,NAC}$) was calculated using the EC2 specification [38], as shown in Equation (6):

$$E_{c,NAC} = 22 \cdot (f_{cm}/10)^{0.3} \quad (6)$$

where f_{cm} is the compressive strength of concrete cylinders.

For the elastic modulus of RAC ($E_{c,RAC}$), the modified model considering the influences of the RCA replacement ratio and the residual mortar content (C_{RM}) was introduced:

$$E_{c,\,RAC} = (1 - 2/3 \cdot r \cdot C_{RM}) E_{c,\,NAC} \quad (7)$$

where C_{RM} generally ranged from 30% to 50% [39]; according to [2], a C_{RM} of 40% was specified for RAC when it was unknown.

2. Compressive Stress–Strain Relationship

Figure 6 demonstrates that both RAC and NAC exhibit a similar compressive stress–strain relationship. Thus, this work uses the unified model proposed by Xiao et al. [40], including the effect of the RCA replacement ratio, as expressed in Equation (8):

$$y = \begin{cases} ax + (3-2a)x^2 + (a-2)x^3 & 0 \le x < 1 \\ \frac{x}{b(x-1)^2 + x} & x \ge 1 \end{cases} \quad (8)$$

where x and y are the relative stress and strain, respectively, defined as Equations (9) and (10):

$$x = \varepsilon_c / \varepsilon_{cm} \quad (9)$$

$$y = \sigma_c / f_{cm} \quad (10)$$

where σ_c and ε_c are the compressive stress and strain, respectively; and f_{cm} and ε_{cm} indicate the compressive strength and the corresponding peak strain, respectively. Coefficients a and b represent the curve shape in the ascending and descending stages, including the influence of the RCA replacement ratio:

$$a = 2.2(0.748 \cdot r^2 - 1.231 \cdot r + 0.975) \quad (11)$$

$$b = 0.8(7.664 \cdot r + 1.142) \quad (12)$$

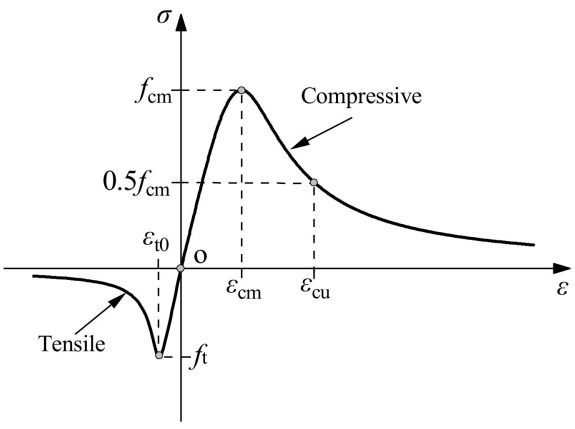

Figure 6. The uniaxial stress–strain curve of concrete.

3. Tensile Stress–Strain Relationship

According to Figure 6, both RAC and NAC exhibit a similar tensile stress–strain relationship. Hence, this study employs the unified model proposed by Xiao et al. [40], including the effect of the RCA replacement ratio, as expressed in Equation (13):

$$y = c \cdot x - (c-1)x^6 \tag{13}$$

where x and y are the relative stress and strain, respectively, defined as Equations (14) and (15):

$$x = \varepsilon_t / \varepsilon_{t0} \tag{14}$$

$$y = \sigma_t / f_t \tag{15}$$

where σ_t and ε_t are the tensile stress and strain, respectively; and f_t and ε_{t0} denote the tensile strength and the corresponding strain, respectively. The coefficient c represents the curve shape, including the influence of the RCA replacement ratio:

$$c = 0.007r + 1.19 \tag{16}$$

Long-Term Properties

1. Long-Term Strain Components

Figure 7 illustrates the concrete strain over time, and the total long-term strain ($\varepsilon_{c,tot}$) of concrete comprises the instantaneous strain (ε_i), the shrinkage strain (ε_{sh}), and the creep strain (ε_{cr}):

$$\varepsilon_{c,tot}(t) = \varepsilon_i(t_0) + \varepsilon_{cr}(t, t_0) + \varepsilon_{sh}(t, t_0) \tag{17}$$

where t (days) is the calculated time of concrete, t_0 (days) indicates the time of the first loading, and t_s denotes the curing period of concrete (days).

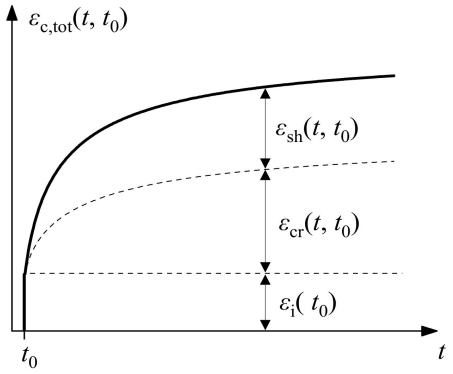

Figure 7. The long-term strain of concrete.

For the concrete subjected to a lower stress state, linear creep deformation is expected with instantaneous deformation via the creep coefficient $\varphi(t, t_0)$:

$$\varepsilon_{cr}(t, t_0) = \varphi(t, t_0) \cdot \varepsilon_i(t_0) \tag{18}$$

The models of the shrinkage deformation and the creep coefficient were introduced into the FE models, as described below.

2. Shrinkage Model

The total shrinkage is composed of the autogenous and drying shrinkage, i.e., $\varepsilon_{sh} = \varepsilon_{sh,au} + \varepsilon_{sh,dry}$. According to EC 2 [38], the autogenous shrinkage model was introduced into NAC, as expressed in Equation (19):

$$\varepsilon_{sh,au}^{NAC}(t) = (1.0 - e^{-0.2t^{0.5}}) \times \varepsilon_{sh,au}^{NAC}(\infty) \tag{19}$$

where $\varepsilon_{sh,au}^{NAC}(t)$ is the autogenous shrinkage at day t, and $\varepsilon_{sh,au}^{NAC}(\infty)$ indicates the final autogenous shrinkage calculated using the characteristic concrete strength at day 28, i.e., f_{ck}:

$$\varepsilon_{sh,au}^{NAC}(\infty) = 2.5 \times (f_{ck} - 10) \times 10^{-6} \quad (20)$$

For the autogenous shrinkage model of RAC, a reduction coefficient factor ($\kappa_{sh,au}$) was introduced into that of NAC, and the detailed model can be obtained from a previous study [2]:

$$\varepsilon_{sh,au}^{RAC}(t) = \kappa_{sh,au} \cdot \varepsilon_{sh,au}^{NAC}(t) \quad (21)$$

This study uses the drying shrinkage models listed in EC2 [38] for NAC, as given by Equation (22):

$$\varepsilon_{sh,dry}^{NAC}(t) = \beta_{sh,dry}(t, t_s) \cdot \kappa_{sh,dry} \varepsilon_{sh,dry,0}^{NAC} \quad (22)$$

where $\varepsilon_{sh,dry}^{NAC}(t)$ indicates the drying shrinkage at day t, $\beta_{sh,dry}(t,t_s)$ is the coefficient of the rate of shrinkage over time, $\kappa_{sh,dry}$ represents a coefficient depending on the notional size of the cross-section (h_0), and $\varepsilon_{sh,dry,0}^{NAC}$ denotes the nominal unrestrained drying shrinkage:

$$\beta_{sh,dry}(t, t_s) = \frac{t - t_s}{(t - t_s) - 0.04\sqrt{h_0^3}} \quad (23)$$

For the drying shrinkage of RAC, our previous studies considered the combined effects of the RCA replacement ratio, the residual mortar content, and the strength of the parent concrete and proposed two coefficients: $\kappa_{sh,a}$, considering the influences of the RCA replacement ratio and the residual mortar content, and $\kappa_{sh,f}$, taking the effect of the strength of the parent concrete into account:

$$\varepsilon_{sh,dry}^{RAC} = \kappa_{sh,f} \cdot \kappa_{sh,a} \cdot \varepsilon_{sh,dry}^{NAC} \quad (24)$$

3. Creep Coefficient Model

This work utilized the creep coefficient model according to EC2 [38], as described in Equations (25)–(27):

$$\varphi(t, t_0) = \varphi_0 \cdot \beta_c(t, t_0) \quad (25)$$

$$\varphi_0 = \varphi_{RH} \cdot \beta(f_{cm}) \cdot \beta_c(t_0) \quad (26)$$

$$\beta_c(t, t_0) = \left[\frac{(t - t_0)}{\beta_H + (t - t_0)}\right]^{0.3} \quad (27)$$

where $\varphi(t,t_0)$ is the creep coefficient, φ_0 indicates the notional creep coefficient, $\beta_c(t,t_0)$ denotes a coefficient that describes the development of creep with time after loading, φ_{RH} represents a factor allowing for the effect of relative humidity on the notional creep coefficient, $\beta(f_{cm})$ is a factor allowing for the effect of the strength of concrete on the notional creep coefficient, $\beta_c(t_0)$ stands for a factor allowing for the effect of the period of loading on the notional creep coefficient, and β_H is a coefficient depending on the relative humidity and the notional member size.

For the creep coefficient model of RAC, this work considers the combined effects of the RCA replacement ratio, the residual mortar content, and the strength of the parent concrete. It proposes two coefficients: K_{RCA}, considering the influences of the RCA replacement ratio and the residual mortar content, and K_{RC}, regarding the impact of the strength of the parent concrete [13]:

$$\varphi_{RAC}(t, t_0) = K_{RCA} K_{RC} \varphi_{NAC}(t, t_0) \quad (28)$$

2.2. Model of Shrinkage and Creep Distribution in Composite Slabs

2.2.1. Model of Shrinkage Distribution through Slab Thickness

According to the slab types, various shrinkage distributions through the slab thickness, namely the uniform shrinkage distribution in the RC slabs and the nonuniform shrinkage distribution in the composite slabs, were obtained in the composite beams. Figure 8 depicts the shrinkage models we proposed for NAC and RAC slabs.

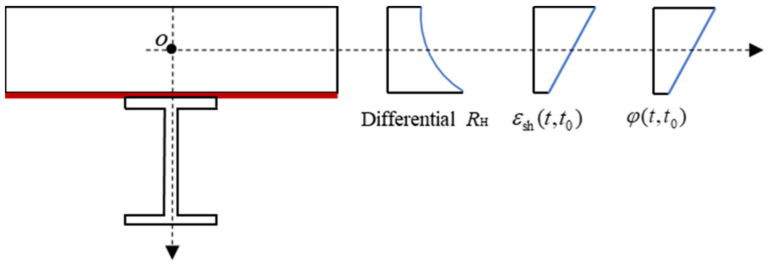

Figure 8. The models of the shrinkage distribution used in the FE model of the composite beams.

Equation (29) is designed for composite beams using RC slabs:

$$\varepsilon_{sh}^{RAC}(t,y) = \varepsilon_{sh,tot}^{RAC}(t,t_s) \tag{29}$$

where t is the calculated days, y indicates the distance from the reference axis, and r denotes the RCA replacement ratio. $\varepsilon_{sh,tot}^{RAC}(t,t_s)$ is the total shrinkage calculated using the notional size of the cross-section according to EC2 [38]; for example, for the solid slab, $h_0 = h$, and Equation (30) calculates $\varepsilon_{sh,tot}^{RAC}(t,t_s)$ as:

$$\varepsilon_{sh,tot}^{RAC}(t,t_s) = \varepsilon_{sh,au}^{RAC}(t) + \varepsilon_{dry,tot}^{RAC}(t,t_s) \tag{30}$$

Equations (21) and (24) also calculate $\varepsilon_{sh,au}^{RAC}(t)$ and $\varepsilon_{dry,tot}^{RAC}(t,t_s)$, respectively.

Equations (31) and (32) are also used for the composite beams with composite slabs:

$$\varepsilon_{sh}^{RAC}(t,y) = f(y,r) \cdot \varepsilon_{sh,tot}^{RAC}(t,t_s) \tag{31}$$

where the function $f(y, r)$ considers the linear influence of the RCA replacement ratio on the shrinkage distribution:

$$f(y,r) = 0.7 - 0.15 \cdot r + \frac{1 + 0.30 \cdot r}{d} \cdot y \tag{32}$$

It is worth noting that the shrinkage distribution model of RAC slabs can degenerate to that of NAC slabs when r equals zero, coinciding with those reported in the literature [25–27].

2.2.2. Creep Coefficient Distribution through Slab Thickness

The long-term creep deformation is reasonably assumed to linearly change with the instantaneous deformation when the stress state is under 40–50% of the concrete strength [38]. To further consider the aging effects of creep, we multiplied the creep coefficient $\varphi(t,t_0)$ by the aging coefficient $\chi(t,t_0)$. This study used a specified value of 0.65 as recommended in [41]:

$$\varepsilon_{cr}(t,t_0) = \chi(t,t_0) \cdot \varphi(t,t_0) \cdot \varepsilon_i(t_0) \tag{33}$$

In other words, Equation (34) calculates the effective modulus, $E_e(t, t_0)$, which is consistent with the AEMM:

$$E_e(t, t_0) = \frac{E_c(t_0)}{1 + \chi(t, t_0)\varphi(t, t_0)} \quad (34)$$

The ambient relative humidity was used to calculate the creep coefficient for the composite beams using RC slabs. In contrast, a nonuniform relative humidity distribution was expected for the composite beams using composite slabs, so a nonuniform creep coefficient distribution was obtained. This study specified the ambient relative humidity on the top surface of the composite slabs but used a relative humidity of 90% on the bottom surface of the composite slabs.

2.3. Element Type and Mesh Discretization

The FE model utilized three types of elements, as shown in Figure 3. The solid C3D8R element was used to simulate the concrete component, the steel beam component, the shear studs, and the loading plates; the shear S4R element was employed to simulate the profiled steel deck; and the truss T3D2 element was utilized to model the reinforcements.

Two types of structured and sweep mesh discretization methods were used. For the loading plates, the web and bottom flange of the steel beam were discretized using the structured method, with a maximum element size of 20 mm. The top flange of the steel beam, the shear studs, the concrete, and the profiled steel decks were discretized using the sweep method. To obtain regulated elements and further improve the convergency efficiency, we used the medial axis algorithm to refine the zone near the shear studs and the advancing front algorithm to refine the other zones. The maximum element size of the flange of the steel beam was 10 mm, and the element size of the profiled steel decks and concrete was in the range of 20–40 mm; an approximate size of 4 mm was selected for the shear studs and their nearby profiled steel decks and concrete. An element size of 20–40 mm was also used for the reinforcements to coordinate with the concrete slabs.

2.4. Boundary Conditions and Interaction Properties

The semi-model of the composite beams was established to enhance the computing efficiency, and the XSYMM symmetric boundary condition was adopted for the symmetric surface, as shown in Figure 9. The support conditions, i.e., the pined or roller support, were determined according to the corresponding test conditions. For the pined supports, the bottom of the steel beam was restrained in all three directions of x, y, and z while for the roller supports, the bottom of the steel beam was restrained in the two directions of x and y.

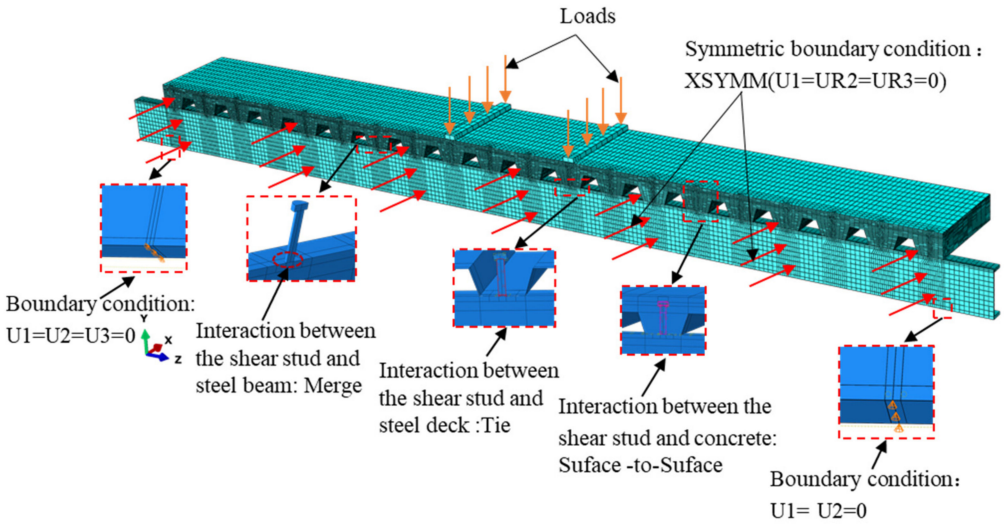

Figure 9. The boundary conditions of typical composite steel–concrete beams.

The surface–surface interactions were used to simulate the behavior of the bonding between the shear studs and the concrete and between the concrete and the profiled steel decks. Table 1 presents the settings of the master and slave surfaces in the FE models. To better simulate the slip between the composite slabs and steel beams, the composite slab and steel beam were modeled in surface–surface interactions. The normal behavior of the interfacial surface was considered the *hard* interaction while a friction factor was used for the tangential behavior of the interfacial surface [42]. Katwal et al. [37] investigated the influence of the friction factor on the flexural behavior of composite beams and reported that a friction coefficient of 0.01 could provide reasonable predictions; thus, this study uses a friction factor of 0.01.

Table 1. The settings of the master surface and slave surface for the face–face interactions.

Surface-to-Surface	Master Surface	Slave Surface
Interaction between the shear stud and the concrete	Shear studs	Concrete
Interaction between the concrete and the profiled steel decks	Profiled steel decks	Concrete
Interaction between the profiled steel decks and the steel beams	Steel beams	Profiled steel decks

The shear studs and the steel beam were merged to simulate the weld. The profiled steel deck was tied with the shear studs and the loading plate with the concrete. The reinforcements were also embedded in the concrete solids.

2.5. Analysis Procedures

The process of the long-term test was usually divided into two stages, as illustrated in Figure 10. Stage I represents the applications of the instantaneous loading on the composite beams, and Stage II indicates the time-dependent evolution of the composite beams under the effects of the sustained external loading and internal shrinkage. This study simulated the long-term behavior of the composite beams by the thermal–mechanical modeling. Indeed, the thermal field simulated the shrinkage effect, and the combined effects of the instantaneous loading and creep were simulated using the AEMM.

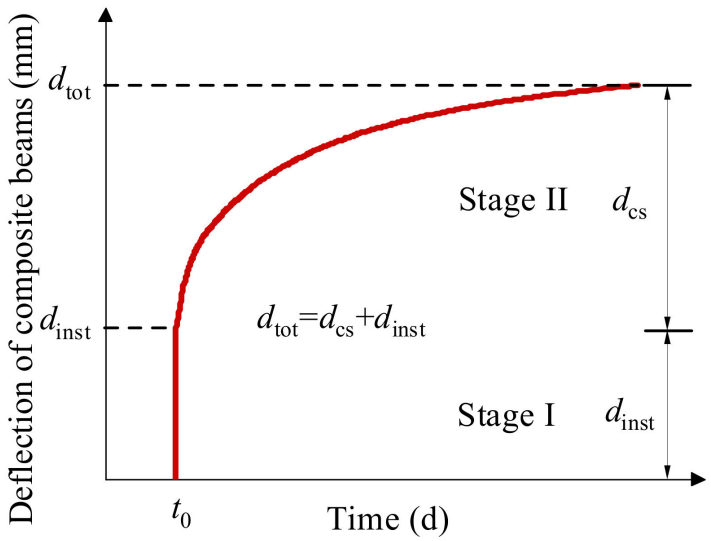

Figure 10. The time-dependent behavior of the composite beams.

Stage I: The instantaneous performance of the composite beams under the short-term loading was modeled, and the mechanical properties of the concrete at time t_0 were adopted.

Stage II: The influence of the shrinkage distribution was first modeled by the temperature variation in the concrete component with an expansion coefficient of 10 με/°C. The sustained loading was substantially applied to the composite beams considering the

shrinkage effects caused by the applied thermal field and the creep effect using the AEMM. The specific process is as follows:

The shrinkage model of Equations (19)–(24) was used to obtain the time-varying value of the concrete shrinkage strain. The coefficient of the expansion of a concrete material as a function of temperature is defined in Abaqus. Using the principle of material shrinkage under cooling, the shrinkage strain of concrete is equal to the shrinkage strain under cooling, and the relationship between concrete shrinkage and temperature is established, and then the relationship between temperature and time is established. The AEMM method was used to obtain the model of the change in the elastic modulus of concrete with time. Based on the variation relationship between temperature and time, the variation model of the concrete elastic modulus with time can be transformed into a variation model with temperature. In Abaqus, *the temperature-dependent data* is used as input to the model of the change of the elastic modulus of concrete with time. By cooling the concrete according to the demand, the simulation of concrete shrinkage and creep deformation can be realized.

3. Validation of FE Models

The long-term experimental investigations conducted on both the flexural and push-out composite beams have great significance for validating the proposed FE models. It is also highlighted that further experimental tests should be conducted on composite steel–RAC beams in the future for benchmark purposes.

3.1. Validation of the FE Model Using the Long-Term Flexural Test Results

To date, no experimental tests have been conducted on the long-term behavior of composite steel–RAC beams, so the test data on composite steel–NAC beams available in the literature was collected. Table 2 lists the test parameters and main results for reference. Specifically, the test specimens included one sample with a composite slab and four samples with RC slabs. The strength of the concrete, the span of the composite beam, and the depth of the slab ranged from 24.5 to 34.0 MPa, 4000 to 8000 mm, and 60 to 125 mm, respectively. The test duration varied from 124 to 1085 days under the sustained loading of 6.4–19.8 kN/m.

3.1.1. Composite Beams with Composite Slabs

Figure 11 compares the measured and numerical data on the composite beams with a composite slab [23]. Samples CSB1 and CSB2 were sustained for 107 days at sustained loads of 7.3 and 16.24 kN/m, respectively. The first loading period was 27 days. The long-term mid-span deflections of CBS1 and CSB2 were measured to be 2.59 and 4.88 mm, respectively, while those computed by the FE model were 2.41 and 4.59 mm, respectively, corresponding to a difference of 6.9% and 5.9%, respectively, between the measured and calculated values. This difference may be due to the average ambient humidity being used in the FE model, which cannot reflect the variation in the relative humidity during the test. The measured and numerical interfacial slips at the end of the specimen due to the long-term shrinkage and creep effects were 0.042 and 0.044 mm, respectively, implying good agreement.

Table 2. The long-term test behavior and the main results of the composite steel–concrete beams.

Sample Label	Steel Beam	Size of Slab			Material Properties		t_0 (Day)	t (Day)	q (kN/m)	$\delta_{cs,EXP}$ (mm)	$\delta_{tot,EXP}$ (mm)	$\delta_{cs,FE}$ (mm)	$\delta_{tot,FE}$ (mm)	$\delta_{cs,FE}/\delta_{cs,EXP}$	$\delta_{tot,FE}/\delta_{tot,EXP}$
		L (mm)	h (mm)	b (mm)	f_{cm} (MPa)	$f_{y,sb}$ (MPa)									
CSB1 [23]	310UB40	8000	125	2000	26.1	332	27	124	7.30	2.59	23.7	2.41	24.2	0.931	1.021
CSB2 [23]	310UB40	8000	125	2000	26.1	332	27	124	16.24	4.88	30.24	4.59	31.55	0.941	1.043
LCB1 [15]	180 × 100 × 4 × 4	4000	60	600	24.5	304	7	1085	7.29	5.63	9.57	5.88	10.24	1.044	1.070
LCB2 [15]	180 × 100 × 4 × 4	4000	60	600	34.0	304	7	1085	7.29	6.11	9.72	6.63	10.91	1.085	1.122
CB1[16]	310UB40	8000	125	2000	27.7	324	—	461	6.40	8.34	21.33	8.84	22.12	1.060	1.037
CB3[16]	310UB40	8000	125	2000	27.7	324	29	222	19.80	12.26	38.66	12.94	42.23	1.055	1.092
Mean value														1.019	1.064
Standard deviation														0.066	0.038

Note: t_0 is the time of the first loading; t indicates the long-term loading time; q denotes a uniformly distributed load considering the self-weight of the load; $\delta_{tot,EXP}$ and $\delta_{tot,FE}$ represent the experimental and numerical total deflection of the composite beams, respectively; $\delta_{cs,EXP}$ and $\delta_{cs,FE}$ stand for the additional deflection due to the shrinkage and creep effects determined by the long-term testing and the numerical modeling, respectively.

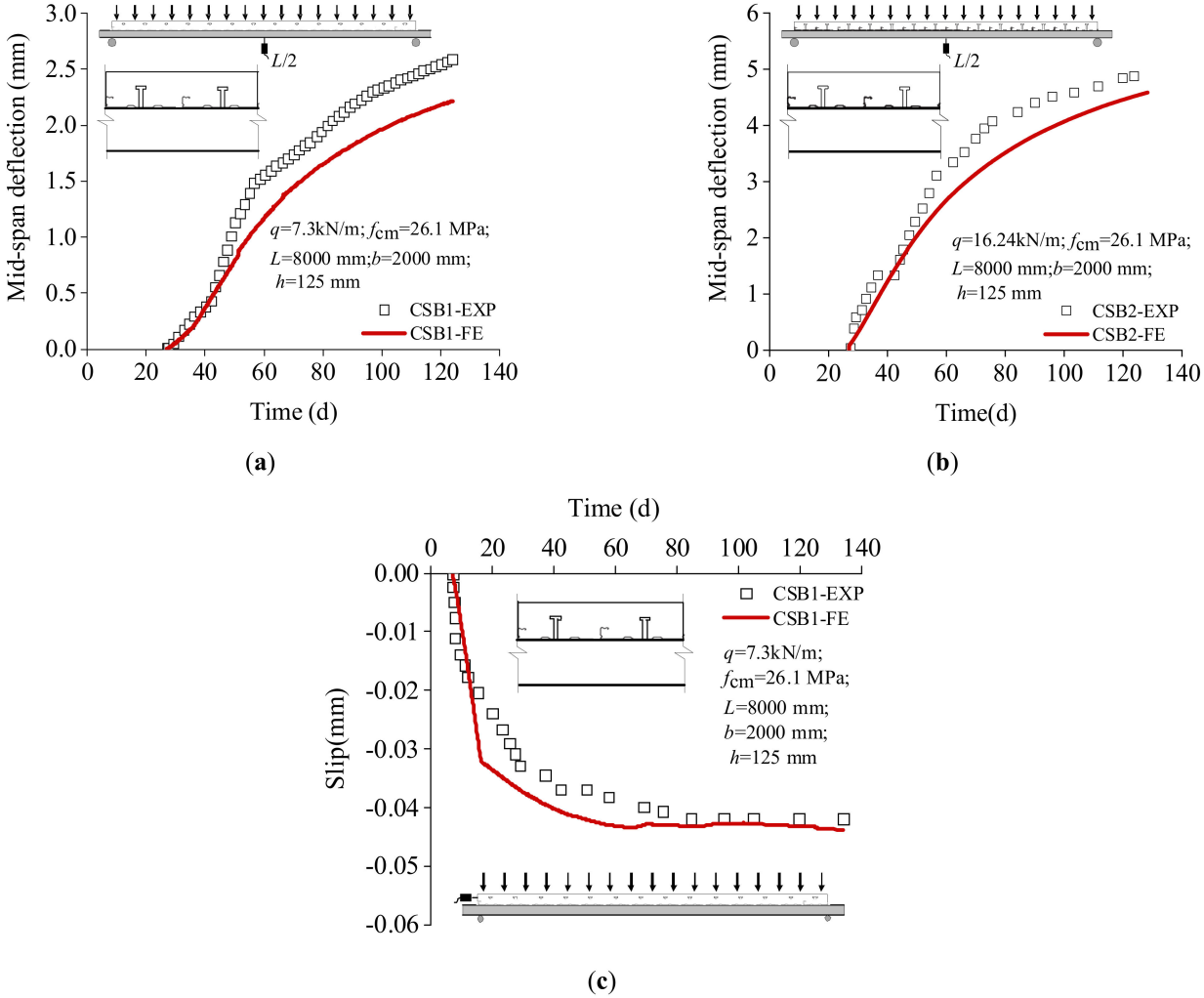

Figure 11. Comparison of the (**a**) CSB1 mid-span deflection, (**b**) CSB2 mid-span deflection, and (**c**) CSB1 relative interface slippage at the end of the specimen of the composite steel–concrete beams with composite slabs determined by the long-term testing and FE modeling.

3.1.2. Composite Beams with RC Slabs

Figure 12 compares the measured and numerical data on the time-dependent deflection of four composite beams with RC slabs. Specifically, LCB1 and LCB2 were collected from [15] and had a concrete compressive strength of 24.5 and 34.0 MPa, respectively; both samples were under long-term loading of 7.29 kN/m for 1078 days. Specimens CB1 and CB3 were obtained from [16]. CB1 was under sustained loading of 6.4 kN/m for 461 days while CB3 was under 19.8 kN/m for 193 days. At the end of their testing, i.e., 1085 days for LCB1 and LCB2, 461 days for CB1, and 222 days for CB3, the measured additional deflections of LCB1, LCB2, CB1, and CB3 were 5.65, 6.11, 8.34, and 12.26 mm, respectively, while the corresponding numerical additional deflections were 5.88, 6.63, 8.84, and 12.94 mm, respectively. The difference between the measured and calculated additional deflections ranged from 4.4% to 8.5%. It is also worth mentioning that although the measured time-dependent deflection of the composite beams with solid slabs varied due to the variation in the environmental conditions, namely the temperature and relative humidity, the FE models could reasonably describe the development of their overall deflection over time.

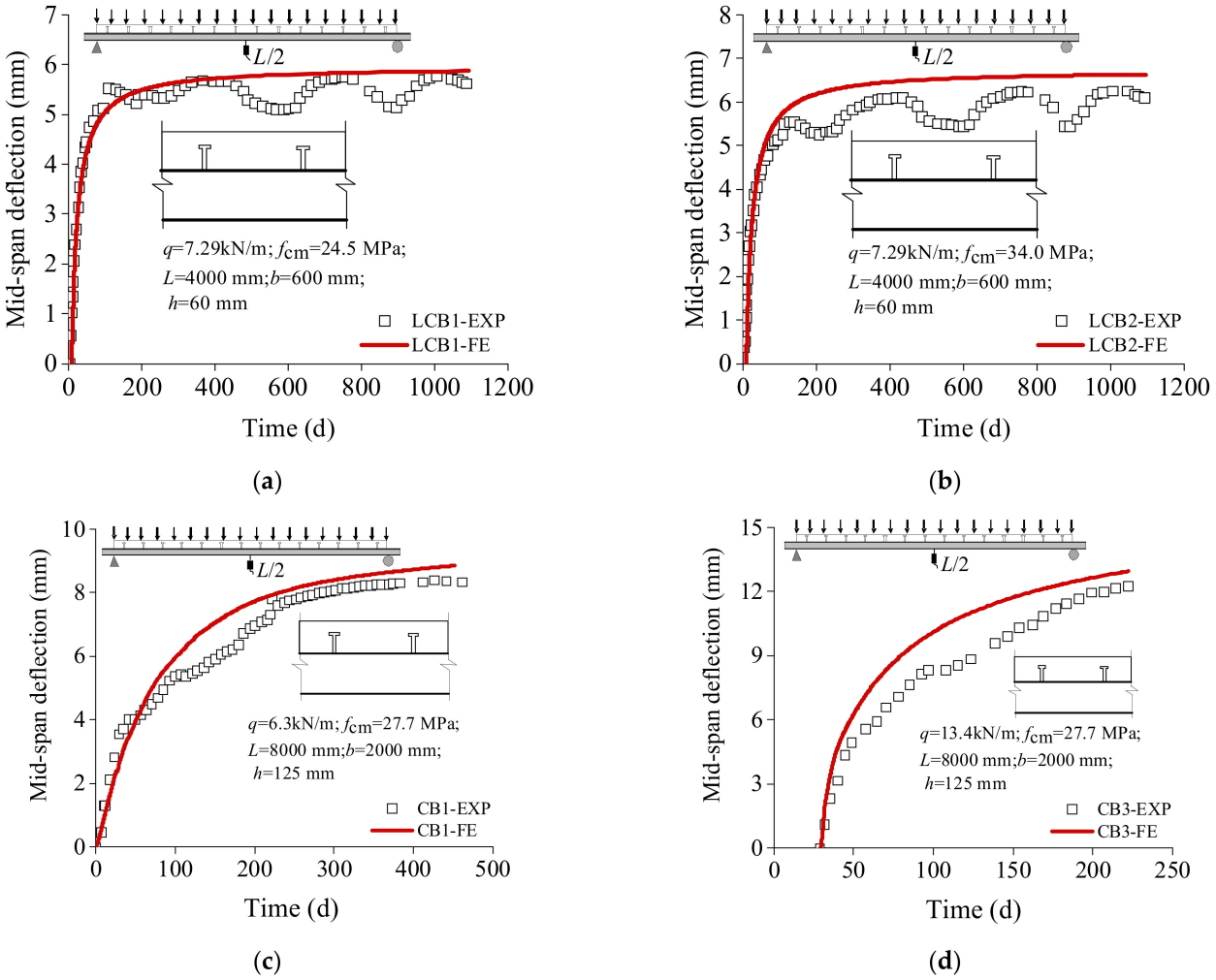

Figure 12. Comparison of the measured and calculated deflections of the composite beams with solid slabs: (**a**) LCB1, (**b**) LCB2, (**c**) CB1, and (**d**) CB3.

Figure 13 compares the measured and calculated strains on the steel beam and the concrete slab. The FE models could reasonably predict the strain development over time for the steel beam and the concrete slab. At the end of their testing, the maximum difference between the measured and calculated strains on the steel beam and the concrete slab was 19.6% and 19.1%, respectively.

Table 2 compares the data on the six samples at the end of their testing. The numerical and measured total long-term deflections of the composite beams had a mean value of 1.064 and a standard deviation of 0.038 while the numerical and measured long-term additional deflections of the composite beams due to the shrinkage and creep effects had a mean value of 1.019 and a standard deviation of 0.066.

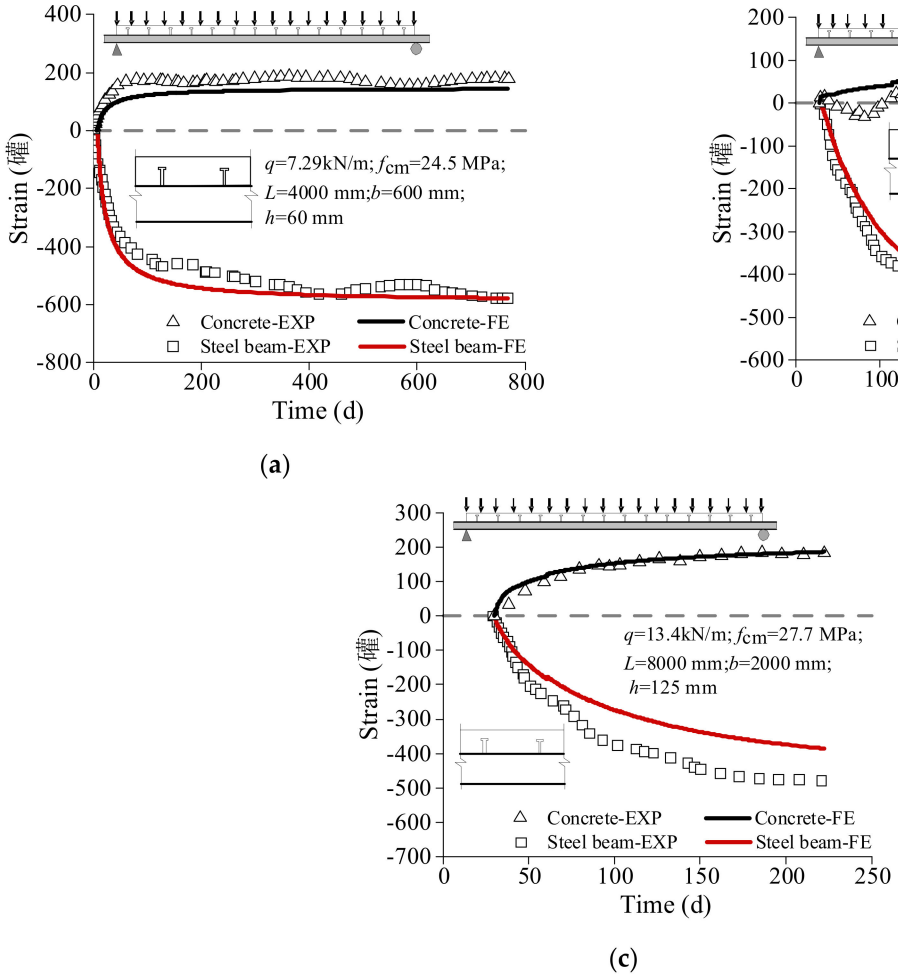

Figure 13. Comparison of the measured and calculated strains at the mid-span of the composite beams with RC slabs: (**a**) LCB1, (**b**) CB1, and (**c**) CB3.

3.2. Validation of the FE Model Using the Long-Term Push-Out Test Results

Figure 14 compares the measured and calculated slip of the composite beam with composite slabs over time using the push-out test. Table 3 tabulates the detailed information on this sample. Although the slip of the composite beam had a narrow range, the FE model predicted it well over time. The difference between the measured and computed instantaneous slip was 6.7% while the difference between the measured and calculated total slip of the composite beam at the end of the test was 10.5%.

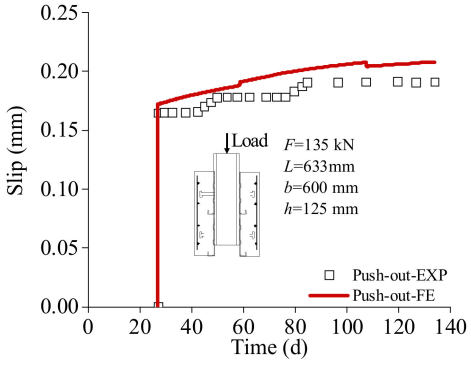

Figure 14. Comparison of the results of the long-term push-out test and FE modeling of composite steel–concrete beams.

Table 3. The long-term push-out test parameters and main results of the composite steel–concrete beams.

Reference	Steel Beam	Size of Slab (mm)			$S_{inst,EXP}$ (mm)	$S_{tot,EXP}$ (mm)	$S_{inst,FE}$ (mm)	$S_{tot,FE}$ (mm)	$S_{inst,FE}/S_{inst,EXP}$	$S_{tot,FE}/S_{tot,EXP}$
		L	h	b						
[23]	**310UB40**	**633**	**125**	**600**	**0.164**	**0.19**	0.175	0.21	1.067	1.105

Note: $S_{inst,EXP}$ and $S_{tot,EXP}$ represent the measured instantaneous slip and total slip, respectively; $S_{cs,FE}$ and $S_{tot,FE}$ indicate the computed instantaneous slip and total slip, respectively.

4. Parametric Study and Design Procedures

The time-dependent behavior of the composite steel–RAC beams was significantly influenced by various factors, so their influence magnitude was quantified using the verified FE models. Furthermore, the design procedures were proposed to predict the time-dependent deflection of composite steel–RAC beams, accounting for the combined effects of uniform (nonuniform) shrinkage, uniform (nonuniform) creep, concrete cracking, and the degree of the shear connection.

4.1. Parametric Study

4.1.1. Parameter Selection

This parametric study selected a simply supported condition for the composite beams. The strength of the concrete was set at 30 MPa, and the reinforcements, with a diameter of 12 mm, were placed at a 200 mm spacing in the longitudinal and transverse directions. The varied parameters included the RCA replacement ratio, the steel decking type, the depth of the slab (h), the beam span-to-depth ratio (L/H), the long-term loading (q), and the ambient relative humidity (R_H). Table 4 lists the parameters and their ranges.

Table 4. The range of the parameters of the FE model.

Parameters	Scope
r (%)	0, 50, 100
h (mm)	120, 135, 150
L/H	9.43, 14.15, 18.87
q (kN/m)	$0.1q_u$, $0.2q_u$, $0.3q_u$
R_H (%)	30, 50, 70
Slab type	Composite slabs, RC slabs

Note: q_u is the ultimate bending strength of the composite beams.

4.1.2. Influence of the RCA Replacement Ratio

Figure 15 delineates the influence of the RCA replacement ratio on the time-dependent deflection of the composite beams, where the composite slabs (using the open-trough steel deck and the clip-pan steel deck) and the RC slabs are considered. The span of the composite beams, the sustained loading, and the relative humidity are 8000 mm, $0.2q_u$, and 50%, respectively. The long-term deflection of the composite beams was enlarged with an increase in the RCA replacement ratio, irrespective of the steel deck types. The long-term deflection of the composite beams with the open-trough steel deck increased by 9.9% and 16.1% when using 50% and 100% RCA, respectively, compared with the reference composite beams with natural coarse aggregate. In fact, the long-term shrinkage and creep deformation rose while the elastic modulus decreased with the incorporation of the RCA into the concrete; both led to an increase in the long-term deflection of the composite beams.

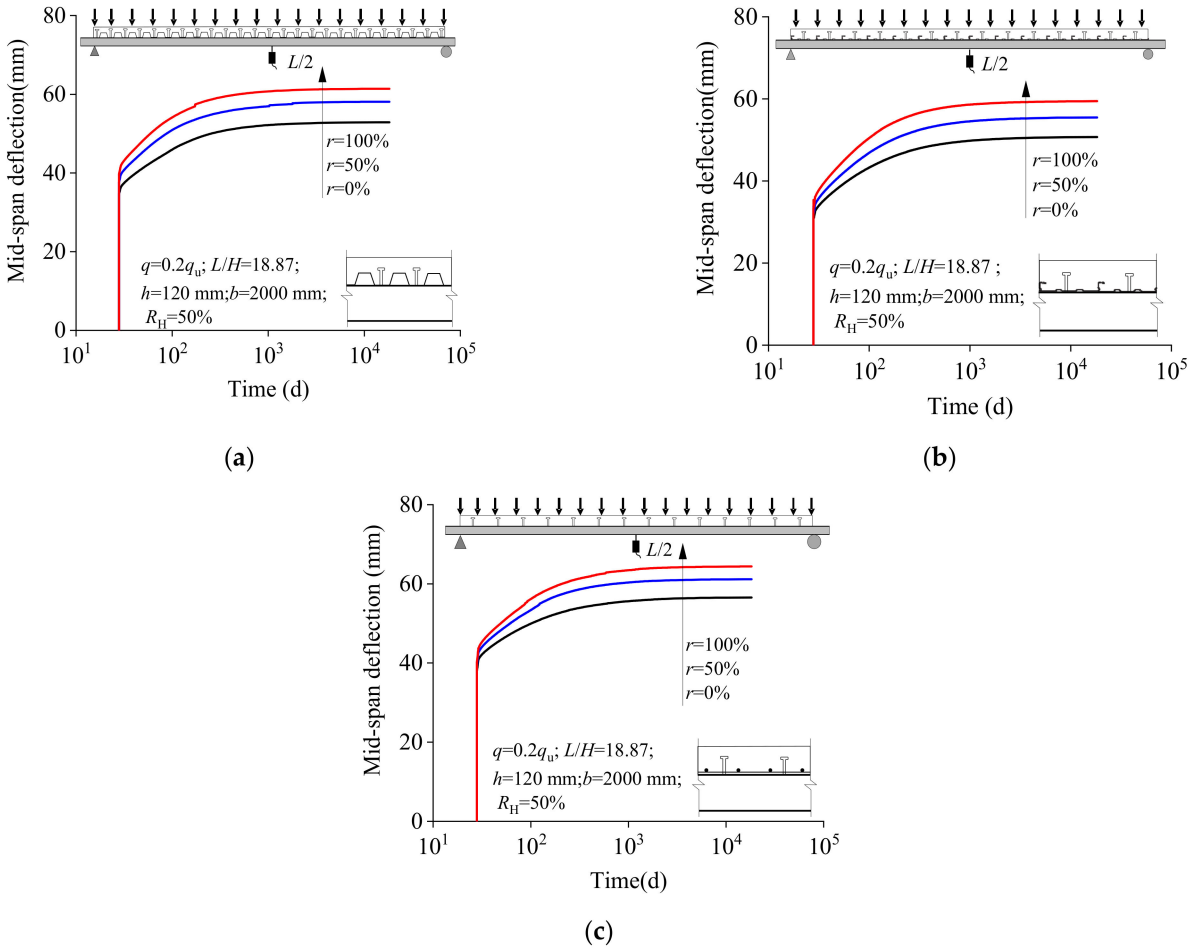

Figure 15. The influence of the RCA replacement ratio on the long-term deflection of the composite beams with (**a**) open-trough composite slabs, (**b**) clip-pan composite slabs, and (**c**) RC slabs.

Figure 16 summarizes the influence of the RCA replacement ratio on the long-term deflection of composite beams with different degrees of shear connection, and in this parametric study, the degree of shear connection ranged from 0.29 to 0.75, which was consistent with values used in practical structures. Clearly, the mid-span deflection of the composite beams increased by 2.2–9.9% and 3.5–17.2% for an RCA replacement ratio of 50% and 100%, respectively, compared to those of the composite beams with NAC.

Furthermore, the long-term deflections of the composite beams due to the shrinkage and creep effects accounted for a remarkable proportion of the total deflection. For an RCA replacement ratio of 0%, 50%, and 100%, the proportion of the shrinkage and creep deflection (δ_{cs}) in the total deflection (δ_{tot}) ranged from 21.6% to 59.7%, 24.1% to 61.5%, and 25.3% to 63.0%, respectively. Thus, a slightly larger proportion was obtained as the RCA replacement ratio rose, indicating that the design of the long-term deflection of composite steel–RAC beams should be taken into further consideration.

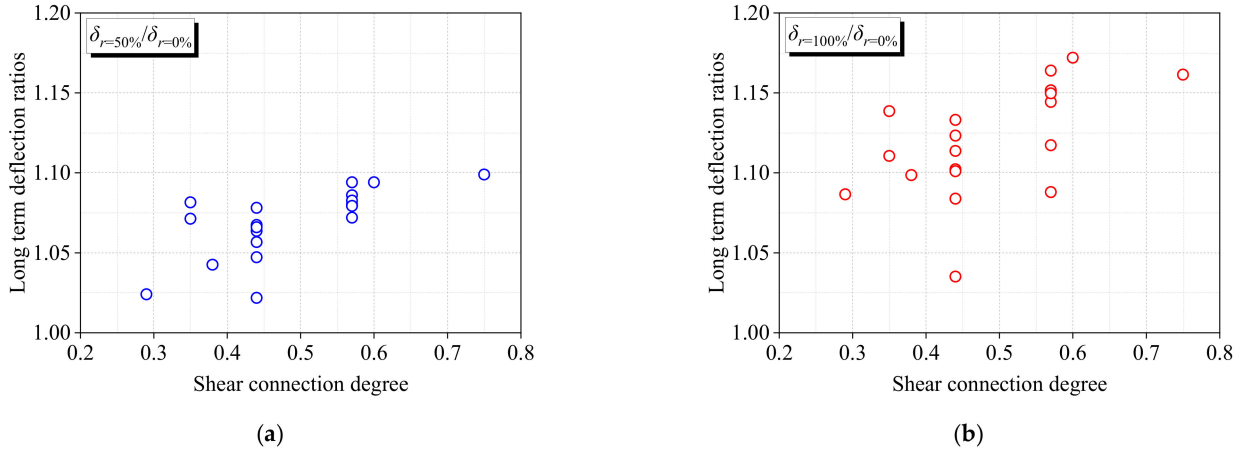

Figure 16. Influence of the RCA replacement ratio on the long-term deflection of composite beams: (**a**) $\delta_{r\ =\ 50\%}/\delta_{r\ =\ 0\%}$ and (**b**) $\delta_{r\ =\ 100\%}/\delta_{r\ =\ 0\%}$.

4.1.3. Influence of the Slab Type

The slab types affected the shrinkage and creep distributions: uniform shrinkage and creep for the RC slabs and nonuniform shrinkage and creep for the composite slabs. Figure 17 demonstrates the influence of the slab types on the time-dependent behavior of the composite beams, and the selected slabs included the RC slab and the composite slab. Both beams were under a sustained loading of $0.2q_u$ and relative humidity of 50% for 50 years. The long-term additional deflection of the composite beams due to the shrinkage and creep effects was more prominent for the RC slab than the composite slab, irrespective of the RCA replacement ratio. Specifically, the long-term additional deflection of the composite beams with the RC slabs increased by 4.5%, 6.6%, and 10.3% compared to that of the composite beams with the composite slabs at an RCA replacement ratio of 0%, 50%, and 100%, respectively, mainly because less humidity distribution was observed for the composite beams with the RC slabs than the composite slabs. Indeed, larger shrinkage-induced force and more considerable creep-induced deformation were expected in the composite beams using the RC slabs. In such a case, for the routine design of composite steel–RAC beams, different shrinkage and creep models should be specified according to the selected slab types: uniform shrinkage and creep for the RC slabs and nonuniform shrinkage and creep for the composite slabs.

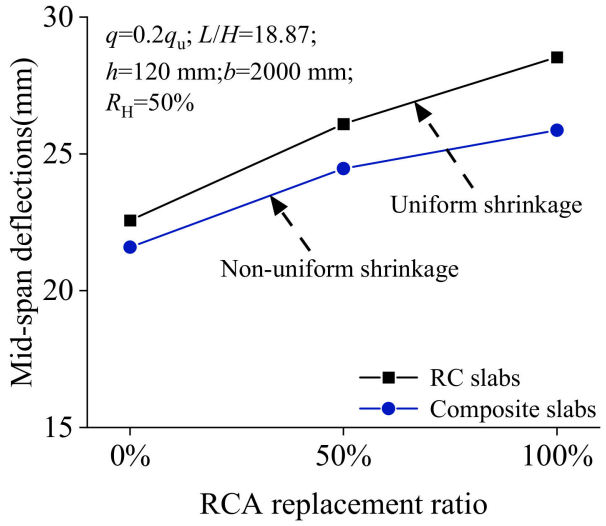

Figure 17. The influence of the slab type on the long-term additional deflection of the composite beams.

4.1.4. Influence of the Slab Depth

Figure 18 shows the variation in the long-term deflection of the composite beams with the depth of the slab. The depth of the slab was 120, 135, and 150 mm for both the open-trough composite slabs and the clip-pan composite slabs. The long-term deflection of the composite beams rose with an increase in the depth of the slab, irrespective of the RCA replacement ratio. For instance, the long-term deflection of the composite beams declined by 6.7% and 13.2% at a slab depth of 135 and 150 mm, respectively, compared to a slab depth of 120 mm for the composite beams with a 100% RCA replacement ratio and open-trough composite slabs. In fact, increasing the depth of the slab enlarged the flexural stiffness but reduced the long-term (shrinkage and creep) deformations, so a smaller deflection of the composite beams was expected.

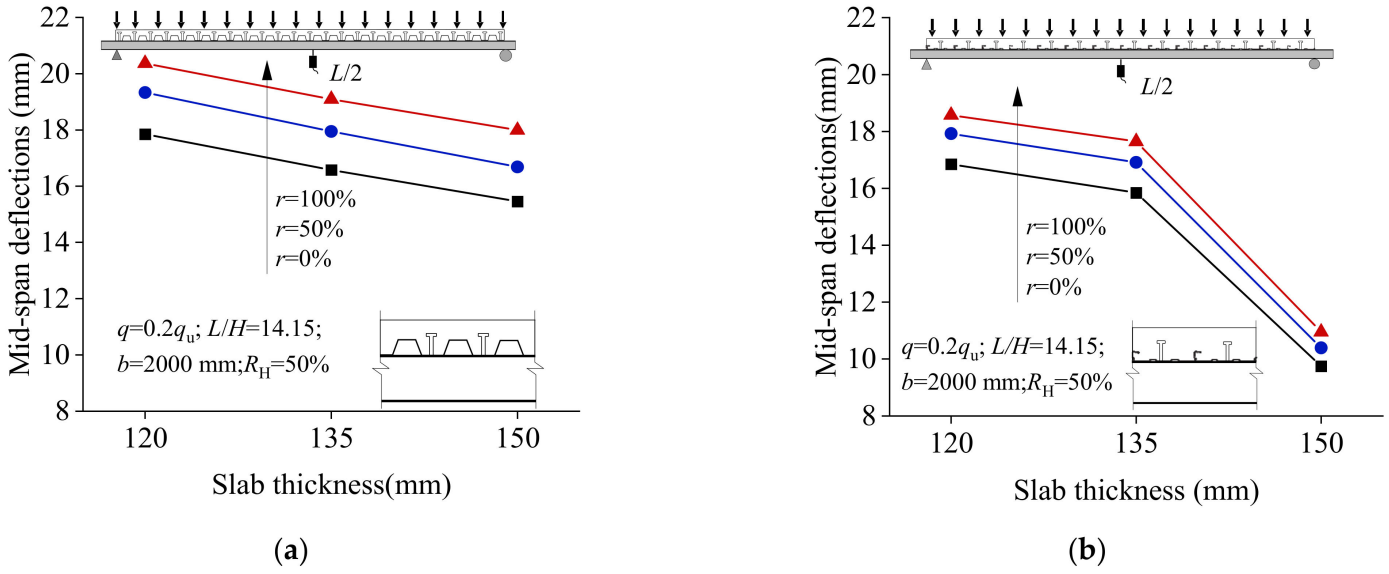

Figure 18. The influence of the depth of the slab on the long-term deflection of the composite beams with the (**a**) open-trough composite slab and (**b**) clip-pan composite slab.

4.1.5. Influence of the Beam Span-to-Depth Ratio

Figure 19 presents the influence of the beam span-to-depth ratio on the long-term deflection of the composite beams, and the beam span-to-depth ratio was selected to be 9.43, 14.15, and 18.87. Both open-trough composite slabs and clip-pan composite slabs were used. The long-term deflection of the composite beams enlarged with an increase in the beam span-to-depth ratio, irrespective of the RCA replacement ratio. Moreover, nonlinear correlations were obtained for the influence of the beam span-to-depth ratio on the long-term deflection of the composite beams. For example, the long-term deflection of the composite beams using 100% RCA and the open-trough composite slabs with a span-to-depth ratio of 18.87 was 2.57 and 9.77 times that of the composite beams with a span-to-depth ratio of 14.15 and 9.43, respectively, because an increase in the beam span-to-depth ratio reduced the flexural stiffness, enlarging the instantaneous, creep-induced, and shrinkage-induced deflections.

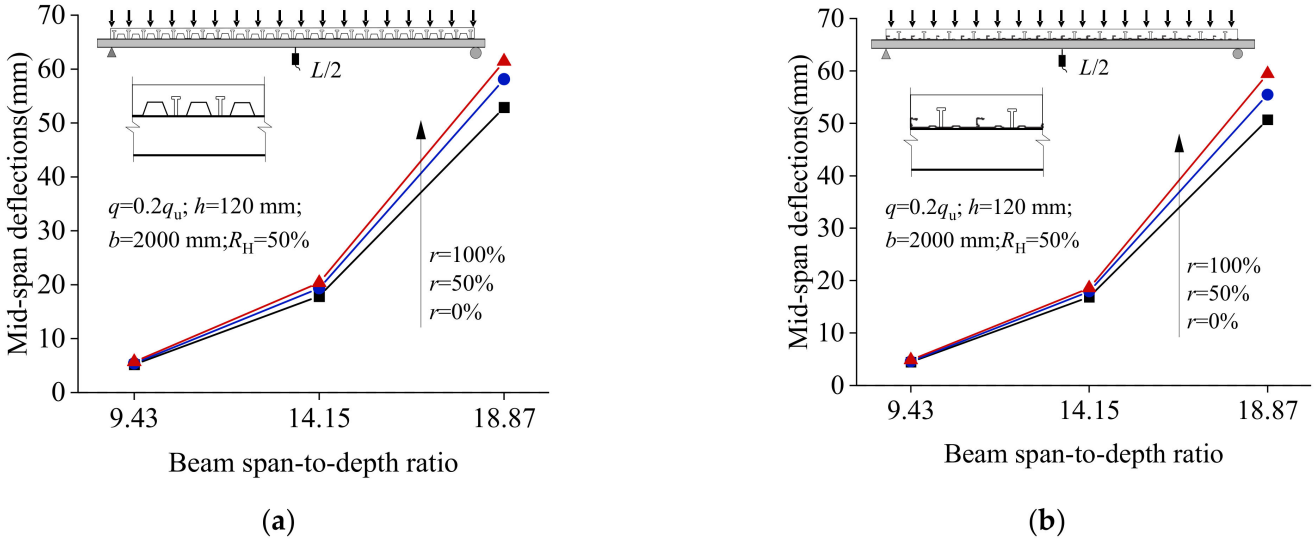

Figure 19. The influence of the beam span-to-depth ratio on the long-term deflection of the composite beams with the (**a**) open-trough composite slab and (**b**) clip-pan composite slab.

4.1.6. Influence of the Long-Term Load Level

Figure 20 illustrates the influence of the sustained loading on the long-term deflection of the composite beams, and the selected loading level was $0.1q_u$, $0.2q_u$, and $0.3q_u$. As expected, the long-term deflection of the composite beams enlarged with an increase in the sustained loading level. The long-term deflection of the composite beams with 100% RCA and the open-trough composite slabs increased by 58.2% and 119.2% at a sustained loading level of $0.2q_u$ and $0.3q_u$, respectively, compared to a sustained loading of $0.1q_u$ because a higher degree of concrete cracking occurred, enlarging the instantaneous and creep-induced deflections.

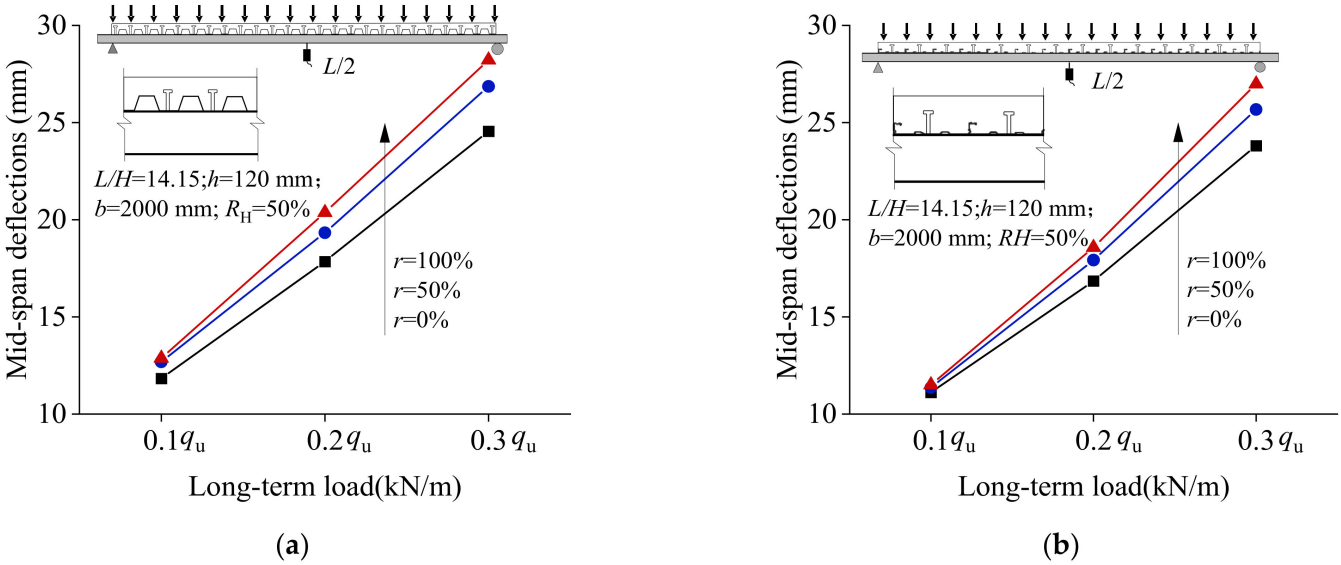

Figure 20. The influence of the sustained loading on the long-term deflection of the composite beams with the (**a**) open-trough composite slab and (**b**) flat composite slab.

4.1.7. Influence of the Relative Humidity

Figure 21 delineates the impact of the ambient relative humidity on the long-term deflection of the composite beams. To this end, the relative humidity of the composite beams with both the open-trough composite slabs and the clip-pan composite slabs ranged from 30% to 70%. The long-term deflection of the composite beams rose with an increase in the relative humidity. The long-term deflection of the composite beams with 100% RCA and the open-trough composite slabs declined by 1.5% and 11.0% at a relative humidity of 50% and 70%, respectively, compared to a relative humidity of 30% since the long-term shrinkage and creep decreased with an increase in the relative humidity, thereby reducing the additional deflection simultaneously.

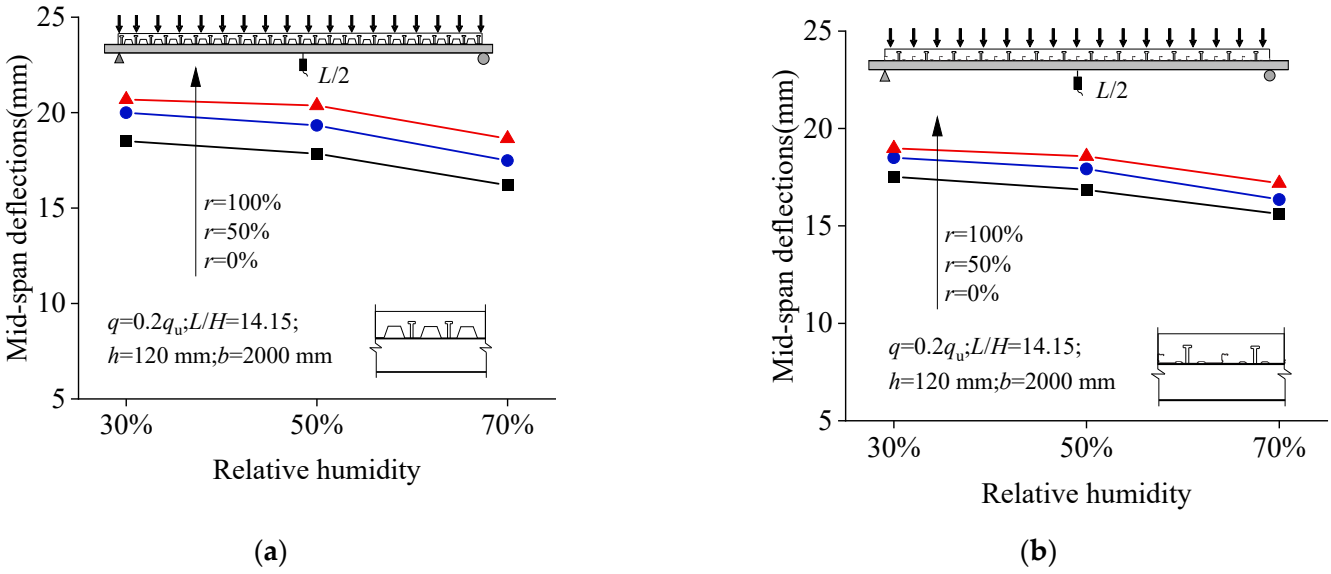

Figure 21. The influence of the ambient relative humidity on medium- and long-term deflection of the composite beams with the (**a**) open-trough composite slab and (**b**) clip-pan composite slab.

4.2. Design Procedures

From the parametric study, one can conclude that the RCA replacement ratio, the slab type, the size of the composite beam, the long-term loading, and the ambient relative humidity could affect the time-dependent behavior of composite beams. However, no design procedures are available to predict the time-dependent behavior of composite beams.

The long-term deflection (δ_{tot}) of composite beams is composed of instantaneous deflection (δ_{inst}), deflection due to the creep effect (δ_{cr}), and deflection due to the shrinkage effect (δ_{sh}) as follows:

$$\delta_{tot} = \delta_{inst} + \delta_{cr} + \delta_{sh} \tag{35}$$

Generally, the instantaneous and creep deflections are calculated following the elastic analysis principle, using a reduced stiffness (B) to consider the influence of the slip, and employing the effective modulus method to account for the creep effect. For example, the instantaneous and creep deflections of a simply supported composite beam under a uniformly distributed loading (q) is calculated by:

$$\delta_{inst} + \delta_{cr} = \frac{5qL^4}{384B} \tag{36}$$

where q is the long-term loading, L indicates the span of the composite beams, and B represents the reduced stiffness considering the slip effect in the composite beams with the partial shear connection.

Some international specifications have been recommended for shrinkage deflection, including the shrinkage deformation of concrete, e.g., 150×10^{-6} or 200×10^{-6} for GB

50017 [43] and 300 × 10^{-6} for EC 4 [44]. It is worth noting that only the uniform shrinkage distribution was included while the nonuniform shrinkage distribution due to the impermeable steel deck was neglected. In this manner, the deflection due to shrinkage was presented through the shrinkage curvature (ξ_{sh}):

$$\xi_{sh} = \frac{\varepsilon_{sh} \cdot E_{sh} \cdot A_{cf} \cdot d_{sh}}{B} \quad (37)$$

As shown in Figure 22, ε_{sh} is the shrinkage deformation at the centroidal axis of the floor slab; it is the uniform shrinkage for the RC slab and is estimated by the nonuniform shrinkage model for the composite slab; A_{cf} denotes the cross-sectional area of the floor slab; d_{sh} represents the distance between the centroidal axial of the slab and the centroidal axial of the composite beams; and E_{sh} indicates the elastic modulus of the concrete considering the shrinkage effect and is calculated according to EC 4 [44], as expressed in Equation (38):

$$E_{sh} = \frac{E_c}{1 + 0.65\varphi} \quad (38)$$

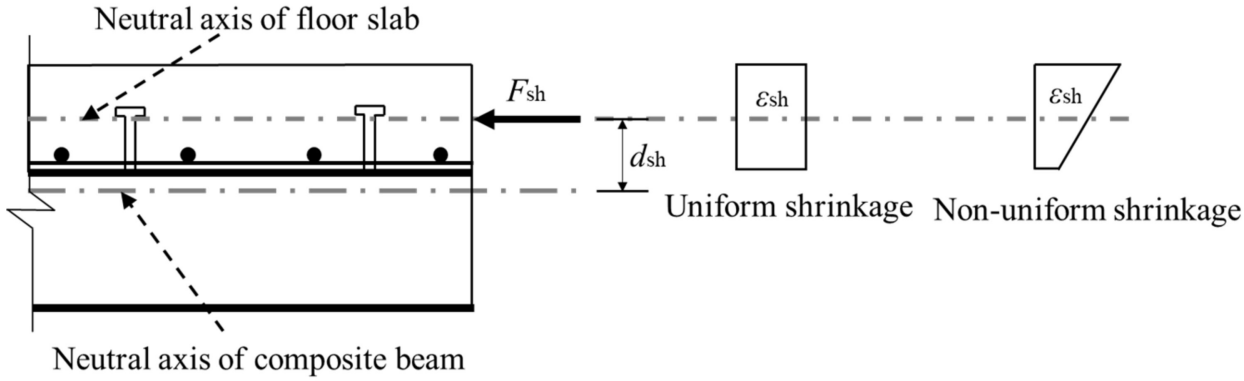

Figure 22. The effect of the concrete shrinkage on the long-term deflection of the composite beams.

For the composite beams with the RC slabs, φ is the creep coefficient calculated using the ambient relative humidity. In contrast, for the composite beams with the composite slabs, φ is the equivalent creep coefficient using the average of the ambient relative humidity and the humidity at the bottom surface of the composite slabs. It is worth mentioning that the shrinkage effect is considered via the external action instead of the internal action.

Equations (35)–(38) calculated the deflections of the composite beams. Figure 23 compares the calculated and numerical deflections of the composite beams at different RCA replacement ratios. It is evident that the design procedures this study proposed could reasonably predict the long-term deflection of composite beams. The mean value of the calculated/numerical long-term deflection of the composite beams was 98.6%, 97.1%, and 96.1% at an RCA replacement ratio of 0%, 50%, and 100%, respectively. The standard deviation of the calculated/numerical long-term deflection of the composite beams was 0.191, 0.198, and 0.194 at an RCA replacement ratio of 0%, 50%, and 100%, respectively.

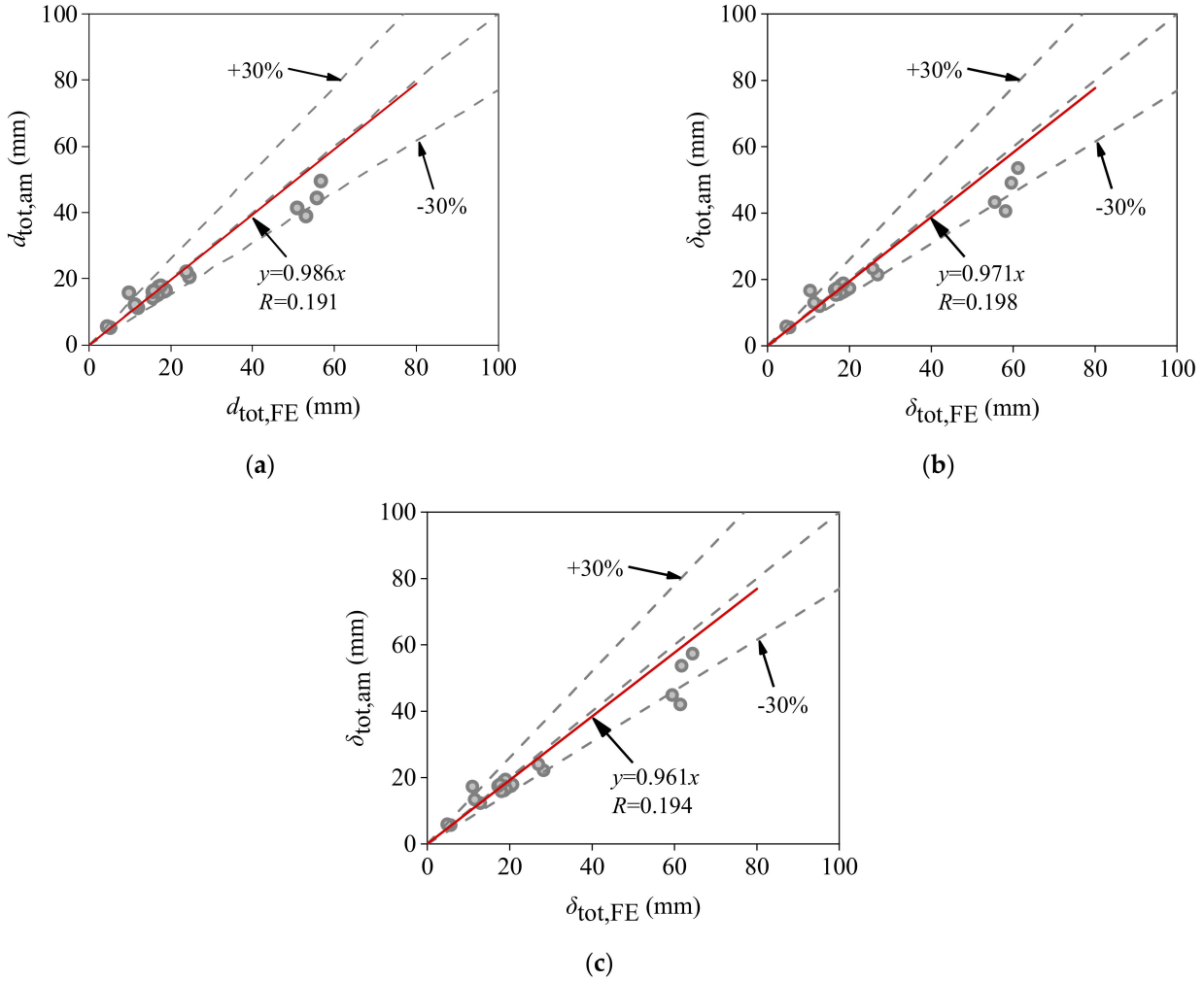

Figure 23. Comparison of the FE results with the calculation results of the modified design method at an RCA replacement ratio of (**a**) 0%, (**b**) 50%, and (**c**) 100%.

5. Conclusions

This study proposed FE models of the time-dependent behavior of composite steel–RAC beams using thermal–mechanical techniques that consider the combined effects of concrete cracking, uniform or nonuniform shrinkage, uniform or nonuniform creep, and the degree of the shear connection. The derived models were benchmarked using available long-term test results from the related literature. A parametric study was conducted to quantify the impact of various factors on the time-dependent behavior of composite steel–RAC beams. Then, the design procedures were proposed by including the deflection component due to shrinkage. The following conclusions can be drawn from the above findings:

- The developed FE models could reasonably predict the time-dependent behavior of composite steel–RAC beams by using a thermal field to simulate the shrinkage distribution and the AEMM to represent the creep effect.
- The RCA replacement ratio significantly influenced the time-dependent behavior of the composite beams. The deflection of the composite beams was enlarged by 2.2–9.9% and 3.5–17.2% at an RCA replacement ratio of 50% and 100%, respectively.
- The composite beams with the RC slabs exhibited uniform shrinkage and creep characteristics while those with the composite slabs exhibited nonuniform shrinkage and creep characteristics. The effect of the slab type on the time-dependent behavior of the composite beams could not be neglected, and the deflection of the composite beams

with the composite slabs was overestimated by 4.5–10.3% when the uniform shrinkage and creep models were used.
- The developed design procedures reasonably predicted the long-term deflection of composite steel–RAC beams, and the mean difference between the calculated and FE results ranged from 0.961 to 0.986 at the different RCA replacement ratios.

Author Contributions: J.Y.: Investigation, Methodology, Software, Formal analysis, Writing, Writing—review, and editing. C.L.: Investigation, Software, Formal analysis, Writing. Q.W.: Methodology, Formal analysis, Writing—review, and editing. Y.G.: Writing—review, and editing. All authors have read and agreed to the published version of the manuscript.

Funding: The research work in this paper was supported by National Natural Science Foundation of China, China (51808351); by Science and Technology Project of MHRUD, China (2019-K-054); by Doctoral Scientific Research Foundation, China (2019-BS-193, 2021-BS-165); by Liaoning Research Project, China (lnjc202007); and by Shenyang Science and Technology Project, China (RC200143).

Institutional Review Board Statement: Not applicable.

Informed Consent Statement: Not applicable.

Data Availability Statement: Not applicable.

Acknowledgments: The research work in this paper was supported by National Natural Science Foundation of China, China (51808351); by Science and Technology Project of MHRUD, China (2019-K-054); by Doctoral Scientific Research Foundation, China (2019-BS-193, 2021-BS-165); by Liaoning Research Project, China (lnjc202007); and by Shenyang Science and Technology Project, China (RC200143).

Conflicts of Interest: The authors declare no conflict of interest.

References

1. Wang, Y.M.; Deng, Z.H.; Xiao, J.Z.; Sheng, J. Mechanical properties of recycled aggregate concrete under multiaxial compression. *Adv. Struct. Eng.* **2020**, *23*, 2529–2538. [CrossRef]
2. Wang, Q.H. Time-Dependent Behaviour of Composite Steel-Concrete Slabs Prepared with Recycled Coarse Aggregate. Ph.D. Thesis, The University of Sydney, Sydney, Australia, 2017.
3. *CECS 273—2010*; Code for Composite Slabs Design and Construction. National Standard of the People's Republic of China. China Planning Press: Beijing, China, 2010.
4. Sindy, S.P.; Belén, G.F.; Fernando, M.A.; Javier, E.L. Flexural performance of reinforced concrete beams made with recycled concrete coarse aggregate. *Eng. Struct.* **2018**, *156*, 32–45. [CrossRef]
5. Rahal, K.N.; Alrefaei, Y.T. Shear strength of longitudinally reinforced recycled aggregate concrete beams. *Eng. Struct.* **2017**, *145*, 273–282. [CrossRef]
6. Arezoumandi, M.; Smith, A.; Volz, J.S.; Khayat, K.H. An experimental study on shear strength of reinforced concrete beams with 100% recycled concrete aggregate. *Eng. Struct.* **2015**, *88*, 154–162. [CrossRef]
7. Fathifazl, G.; Razaqpur, A.G.; Isgor, O.B.; Abbas, A.; Fournier, B.; Foo, S. Shear capacity evaluation of steel reinforced recycled concrete (RRC) beams. *Eng. Struct.* **2011**, *33*, 1025–1033. [CrossRef]
8. Zhang, J.W.; Liu, F.F.; Kazoza, E.; Cao, W.L. Experimental study on flexural behavior of recycled coarse aggregate concrete composite beams with closed section steel deck. *J. Harbin Inst. Technol.* **2015**, *47*, 86–92. [CrossRef]
9. Wang, Q.H.; Geng, Y.; Wang, Y.Y.; Zhang, H. Drying shrinkage model for recycled aggregate concrete accounting for the influence of parent concrete. *Eng. Struct.* **2020**, *202*, 109888. [CrossRef]
10. Zhang, H.; Wang, Y.Y.; Lehman, D.E.; Geng, Y.; Kuder, K. Time-dependent drying shrinkage model for concrete with coarse and fine recycled aggregate. *Cem. Concr. Compos.* **2019**, *105*, 103426. [CrossRef]
11. Sindy, S.P.; Beln, G.F.; Fernando, M.A.; Iris, G.T. Time-dependent behaviour of structural concrete made with recycled coarse aggregates. Creep and shrinkage. *Constr. Build. Mater.* **2016**, *122*, 95–109. [CrossRef]
12. Geng, Y.; Zhao, M.Z.; Yang, H.; Wang, Y.Y. Creep model of concrete with recycled coarse and fine aggregates that accounts for creep development trend difference between recycled and natural aggregate concrete. *Cem. Concr. Compos.* **2019**, *103*, 303–317. [CrossRef]
13. Geng, Y.; Wang, Y.Y.; Chen, J. Creep behaviour of concrete using recycled coarse aggregates obtained from source concrete with different strengths. *Constr. Build. Mater.* **2016**, *128*, 199–213. [CrossRef]
14. Xue, W.C.; Ding, M.; He, C.; Li, J. Long-term behavior of prestressed composite beams at service loads for one year. *J. Struct. Eng.* **2008**, *134*, 930–937. [CrossRef]

15. Fan, J.S.; Nie, J.G.; Li, Q.W.; Wang, H. Long-term behavior of composite beams under positive and negative bending. i: Experimental study. *J. Struct. Eng.* **2010**, *136*, 849–857. [CrossRef]
16. Al-deen, S.; Ranzi, G.; Vrcelj, Z. Full-scale long-term experiments of simply supported composite beams with solid slabs. *J. Constr. Steel Res.* **2011**, *67*, 308–321. [CrossRef]
17. Zhang, S.P.; Chen, X.; Li, G.L. Study on the influence of reinforcement on creep and shrinkage effects of composite beams. *IOP Conf. Ser. Earth Environ. Sci.* **2019**, *267*, 032068. [CrossRef]
18. Wright, H.; Vitek, J.; Rakib, S.N. Long-term creep and shrinkage in composite beams with partial connection. *Proc. Inst. Civ. Eng. Struct. Build.* **1992**, *94*, 187–195. [CrossRef]
19. Ranzi, G. Short- and long-term analyses of composite beams with partial interaction stiffened by a longitudinal plate. *Steel Compos. Struct.* **2006**, *6*, 237–255. [CrossRef]
20. Reginato, L.; Tamayo, J.L.P.; Morsch, I.B. Finite element study of effective width in steel-concrete composite beams under long-term service loads. *Lat. Am. J. Solids Struct.* **2018**, *15*, 1–25. [CrossRef]
21. Erkmen, E.E.; Bradford, M.A. Time-dependent creep and shrinkage analysis of composite beams curved in-plan. *Comput. Struct.* **2011**, *89*, 67–77. [CrossRef]
22. Xiang, T.Y.; Yang, C.; Zhao, G.Y. Stochastic creep and shrinkage effect of steel-concrete composite beam. *Adv. Struct. Eng.* **2015**, *18*, 1129–1140. [CrossRef]
23. Al-Deen, S.; Ranzi, G.; Vrcelj, Z. Full-scale long-term and ultimate experiments of simply-supported composite beams with steel deck. *J. Constr. Steel Res.* **2011**, *67*, 1658–1676. [CrossRef]
24. Ranzi, G.; Leoni, G.; Zandonini, R. State of the art on the time-dependent behaviour of composite steel-concrete structures. *J. Constr. Steel Res.* **2013**, *80*, 252–263. [CrossRef]
25. Wang, Q.H.; Yang, J.S.; Liang, Y.Z.; Zhang, H.; Zhao, Y.; Ren, Q.X. Prediction of time-dependent behaviour of steel-recycled aggregate concrete (RAC) composite slabs via thermo-mechanical finite element modelling. *J. Build. Eng.* **2020**, *29*, 101191. [CrossRef]
26. Wang, Q.H.; Yang, J.S.; Liang, Y.Z.; Zhang, Y.Z.; Fang, Y.F. Time-dependent flexural performance and design procedures for steel-bars truss slabs. *Mag. Concr. Res.* **2020**, *73*, 904–918. [CrossRef]
27. Wang, Q.H.; Ranzi, G.; Wang, Y.Y.; Geng, Y. Long-term behaviour of simply-supported steel-bars truss slabs with recycled coarse aggregate. *Constr. Build. Mater.* **2016**, *116*, 335–346. [CrossRef]
28. Wang, Q.H.; Yang, J.S.; Zhang, Y.Z.; Fang, Y.F.; Ren, Q.X. Analysis and design of long-term responses of simply-supported steel–concrete composite slabs. *J. Build. Eng.* **2022**, *53*, 104496. [CrossRef]
29. Zhang, H.; Wang, Y.Y.; Wang, Q.H.; Geng, Y. Experimental study and prediction model for non-uniform shrinkage of recycled aggregate concrete in composite slabs. *Constr. Build. Mater.* **2022**, *329*, 127142. [CrossRef]
30. Guo, L.H.; Liu, Y.; Qu, B. Fully composite beams with U-shaped steel girders: Full-scale tests, computer simulations, and simplified analysis models. *Eng. Struct.* **2018**, *177*, 724–738. [CrossRef]
31. Nie, J.G.; Cai, C.S. Steel-concrete composite beams considering shear slip effects. *J. Struct. Eng.* **2003**, *129*, 495–506. [CrossRef]
32. Oehlers, D.; Sved, G. Composite beams with limited-slip-capacity shear connectors. *J. Struct. Eng.* **1995**, *121*, 932–938. [CrossRef]
33. Liu, H.B.; Liu, W.H.; Zhang, Y.L. Calculation analysis of shearing slip for steel-concrete composite beam under concentrated load. *Appl. Mech. Mater.* **2005**, *26*, 735–740. [CrossRef]
34. Nie, J.G.; Cai, C.S.; Zhou, T.R.; Li, Y. Experimental and analytical study of prestressed steel-concrete composite beams considering slip effect. *J. Struct. Eng.* **2007**, *133*, 530–540. [CrossRef]
35. Fu, G.; Cui, W. Experimental research on the composite steel-concrete beams with partial shear connection. *Appl. Mech. Mater.* **2011**, *71–78*, 954–958. [CrossRef]
36. Yuan, H.; Yang, Y.; Deng, H.; Yi, W.J. Element-based stiffness reduction coefficient of steel-concrete composite beams with interface slip. *Mater. Struct.* **2016**, *49*, 5021–5029. [CrossRef]
37. Katwal, U.; Tao, Z.; Hassan, M.K. Finite element modelling of steel-concrete composite beams with profiled steel sheeting. *J. Constr. Steel Res.* **2018**, *146*, 1–15. [CrossRef]
38. *BS/EN 1992-1-1*; Eurocode 2: Design of Concrete Structures, Part1-1: General Rules and Rules for Building. The European Committee for Standardization (CEN): Brussels, Belgium, 2004.
39. Juan, M.S.D.; Gutierrez, P.A. Study on the influence of attached mortar content on the properties of recycled concrete aggregate. *Constr. Build. Mater.* **2009**, *23*, 872–877. [CrossRef]
40. Xiao, J.Z.; Li, W.G.; Fan, Y.H.; Huang, X. An overview of study on recycled aggregate concrete in China (1996–2011). *Constr. Build. Mater.* **2012**, *31*, 364–383. [CrossRef]
41. Gilbert, R.I.; Ranzi, G. *Time-Dependent Behaviour of Concrete Structures*; CRC Press: London, UK, 2011.
42. El-Zohairy, A.; Salim, H.; Fawzy, H.; Mustafa, S.; Shihy, A. Finite element modeling of externally post-tensioned composite beams. *J. Build. Eng.* **2015**, *20*, 04015018. [CrossRef]
43. *GB 50017-2017*; Code for Design of Steel Structures. National Standard of the People's Republic of China. China Planning Press: Beijing, China, 2017.
44. *BS/EN 1994-1-1*; Eurocode 4: Design of Composite Steel and Concrete Structures-Part 1-1: General Rules and Rules for Buildings. The European Committee for Standardization (CEN): Brussels, Belgium, 2009.